Article

Journal of Intelligent Material Systems and Structures

Journal of Intelligent Material Systems and Structures
23(2) 183–199

DOI: 10.1177/1045389X11432656
jim.sagepub.com
SAGE

Nonlinear nonconservative behavior and modeling of piezoelectric energy harvesters including proof mass effects

Samuel C Stanton[1], Alper Erturk[3], Brian P Mann[2], Earl H Dowell[2] and Daniel J Inman[4]

Abstract

Nonlinear piezoelectric effects in flexural energy harvesters have recently been demonstrated for drive amplitudes well within the scope of anticipated vibration environments for power generation. In addition to strong softening effects, steady-state oscillations are highly damped as well. Nonlinear fluid damping was previously employed to successfully model drive dependent decreases in frequency response due to the high-velocity oscillations, but this article instead harmonizes with a body of literature concerning weakly excited piezoelectric actuators by modeling nonlinear damping with nonconservative piezoelectric constitutive relations. Thus, material damping is presumed dominant over losses due to fluid-structure interactions. Cantilevers consisted of lead zirconate titanate (PZT)-5A and PZT-5H are studied, and the addition of successively larger proof masses is shown to precipitate nonlinear resonances at much lower base excitation thresholds while increasing the influence of higher-order nonlinearities. Parameter identification results using a multiple scales perturbation solution suggest that empirical trends are primarily due to higher-order elastic and dissipation nonlinearities and that modeling linear electromechanical coupling is sufficient. This article concludes with the guidelines for which utilization of a nonlinear model is preferred.

Keywords

Energy harvesting, piezoelectric, structural health monitoring, sensor, ferroelectric, actuator

Introduction

Piezoelectric energy harvesting has matured as a topic of consistent theoretical and experimental investigation. In particular, the bimorph harvester has been prolifically studied. This type of energy harvester is typically a cantilevered beam consisted of an electrically neutral substrate material with symmetric electroelastic laminates. A proof mass may be attached to tune the resonant frequency of the device upon coupling to a power conditioning circuitry to extract the optimal amount of power from an ambient source of mechanical motion.

It is widely accepted that the linear piezoelectric constitutive relations are valid for weakly excited harvesters. However, several recent studies have shown otherwise (Stanton et al., 2010a, 2010b; Stanton and Mann). This article provides a comprehensive modeling approach and experiment to investigate the validity of modeling linear behavior within piezoceramics. To first set the context, however, we review the relevant history of piezoelectric harvester modeling.

Sodano et al. (2004) and DuToit et al. (2005) were among the first to publish theoretical models for the linear dynamics of piezoelectric energy harvesters with experimental validation. Sodano et al. (2004) generalized several approaches for piezoelectric sensors and actuators (Crawley and Anderson, 1990; Hagood et al., 1990; Smits et al., 1991) to an energy-harvesting scheme and showed that damping effects of power harvesting follow that of a resistive shunt. DuToit et al. (2005) closely followed this work with a lengthy and detailed exposition encompassing not only a variational approach to modeling but also various microelectromechanical system (MEMS) fabrication and design issues,

[1]US Army Research Office, Durham NC, USA
[2]Department of Mechanical Engineering, Duke University, Durham, NC, USA
[3]G. W. Woodruff School of Mechanical Engineering, Georgia Institute of Technology, Atlanta, GA 30332-0405
[4]Department of Aerospace Engineering, University of Michigan, Ann Arbor, MI

Corresponding author:
Samuel C Stanton, US Army Research Office, Durham NC USA
Email: samuel.c.stanton2.civ@mail.mil

resonance versus antiresonance, and nontrivial proof mass kinematics. Later, instead of the Rayleigh–Ritz approach in the study by Sodano et al. (2004) and DuToit et al. (2005), Jiang et al. (2005) solved the eigenvalue problem for a flexural energy harvester with a point mass approximation from the governing partial differential equations where the electromechanical coupling appears in the natural boundary conditions. The exact electromechanical resonance point is derived from a determinant equation, and the ensuing analysis focused on optimal impedance loads, bimorph geometry, and proof mass size for increased power densities. Erturk and Inman (2008a, 2009a) later published linear models for both unimorph and bimorph harvesters transmitting a proof mass and both a translational and a small rotary base excitation. The same authors addressed errors stemming from single-degree-of-freedom (SDOF) models (Erturk and Inman, 2009b) and other questionable results (Erturk and Inman, 2008b, 2008c).

While the preceding articles have formed a basis for accurate energy harvester models, several recent articles have explicitly focused on proof mass effects. Kim et al. (2010) published experimental results confirming the validity of the theory presented in the study by DuToit et al. (2005) with a macroscopic device and two different nonsymmetric proof masses. Yu et al. (2010) also studied nonsymmetric proof masses but added nonvanishing longitudinal displacement and rotary inertia within the cantilever itself in the theoretical model. Finite element methods were used to solve the equations of motion, and a point mass assumption, as expected, inaccurately captured the resonance. Interestingly, the experimental data from both articles show poor correlation in some instances with the linear modeling. In fact, Kim et al. (2010) suggest that nonlinear piezoelectric effects were the culprit, while Yu et al. (2010) do not hypothesize why their data exhibit a clear softening and reduced amplitude effects reminiscent of nonlinear damping (see Figure 7 in the study by Yu et al. (2010)).

Piezoelectric nonlinearity in a harvester was first studied by Hu et al. (2006). A numerical analysis of a piezoelectric plate showed a hardening response due to thickness/shear mode vibration. The physical basis for their model was the cubic theory of nonlinear electroelasticity (Maugin, 1985; Tiersten, 1993; Yang, 2005) but with linear dissipation and linear coupling. Nonlinear coupling in the context of piezoelectric beam actuators was modeled by Von Wagner and Hagendorn (2002), and the nonlinear response to weak electric fields was explained by a combination of nonlinear elastic and coupling phenomena. Triplett and Quinn (2009) theoretically studied the influence of nonlinear strain-dependent coupling in harvesters. While the investigation utilized parameters that yielded hardening responses, harvester piezoceramics typically exhibit softening curves (Priya et al., 2001; Stanton et al., 2010a, 2010b). Nevertheless, the nonlinear coupling could indeed influence already nonlinear resonance curves due to elastic effects. In all aforementioned analyses, however, linear mechanical dissipation is presumed. Stanton et al. (2010a, 2010b) studied the nonlinear response of bimorph harvesters both theoretically and experimentally and modeled nonlinear damping through quadratic air drag. However, without a detailed analysis of the fluid loading in the experiments, it is difficult to maintain confidence that this is the primary source of dissipation.

Motivated by empirical trends and the existing literature concerning weakly excited piezoelectric materials, this article seeks to comprehensively model both nonlinear elasticity and dissipation in piezoelectric energy harvesters. The section titled "Nonlinear and nonconservative modeling" provides a derivation of a SDOF model from Rayleigh–Ritz methods for the piezoelectric harvester to include higher-order piezoelectric relations and nonconservative work expressions. Experimental validation is presented next and followed by metrics for which utilization of a nonlinear model is preferred in the section titled "Linear versus nonlinear modeling." The section titled "Summary and conclusions" provides a summary and a list of our main conclusions along with the directions for future work.

Nonlinear and nonconservative modeling

This section employs the Rayleigh–Ritz procedure to derive a SDOF model for the harvester. In the Rayleigh–Ritz procedure, a modal expansion of the spatiotemporal deflection of a cantilever beam is substituted into the appropriate conservative and nonconservative energy expressions, and subsequent application of Hamilton's extended principle yields governing ordinary differential equations. Provided that our experimental devices are excited within close proximity of the first resonance of the coupled electromechanical system, a single-mode approximation is presumed to be sufficiently accurate for modeling and identification purposes.

Figure 1 illustrates a prototypical harvester consisted of a bimorph cantilever beam with an attached mass. The harvester is composed of a brass shim of thickness h_p with symmetric piezoelectric laminates of thickness h_p each. The transverse deflection is described by the coordinate $w(x,t)$ and is subject to a base displacement $z(t)$. A proof mass is affixed such that the center of mass is at the tip of the beam. The kinetic energy is distributed through the volume of the cantilever as

$$\mathcal{T} = \frac{1}{2}\rho_b \int_{V_b} (\dot{w}+\dot{z})^2 \mathrm{d}V_b + \frac{1}{2}\rho_p \int_{V_p} (\dot{w}+\dot{z})^2 \mathrm{d}V_p \qquad (1)$$

where $w(x,t)$ is the transverse deflection, ρ_b, ρ_p, V_b, and V_p are the respective material densities and total volume

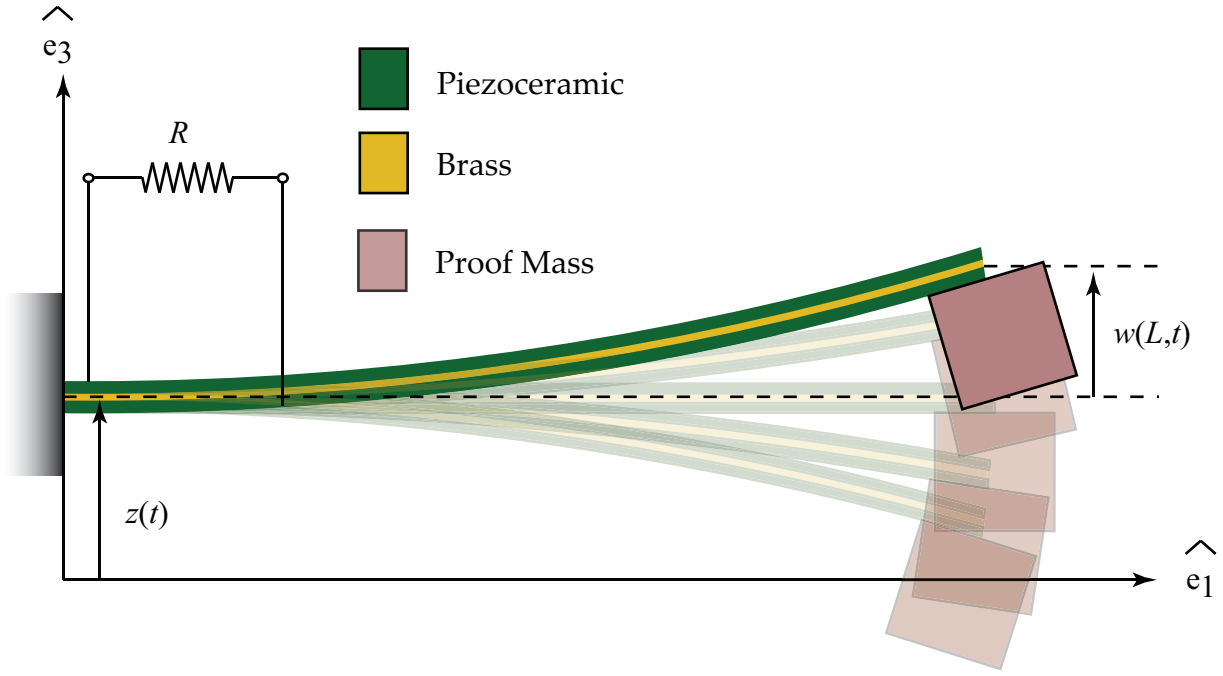

Figure 1. Illustration of the energy harvester studied. The cantilever is excited by a base motion $z(t)$ and transversely deflects a distance of $w(x,t)$.

for the brass substrate and piezoelectric laminates. The cross section of the cantilever is rectangular with width b and total thickness of $h_s + 2h_p$, where h_s is the thickness of the substrate, and h_p is the thickness of the individual piezoelectric laminates. To formulate the kinetic energy of the rigid body at the boundary, consider a position vector from the base of the cantilever to center of mass to the proof mass. Considering Figure 2, this vector may be written as

$$\mathbf{r}_{M_t} = \left[L + o_x w'(L,t)\right]\hat{\mathrm{e}}_1 + \left[z + w(L,t) - \left(o_x + h_p + \tfrac{1}{2}h_s\right)\right]\hat{\mathrm{e}}_3 \tag{2}$$

where the kinematic assumptions reflect negligible longitudinal motion and first-order rotations (i.e. $\cos\theta \approx 1$ and $\sin\theta \approx \theta$). The proof mass kinetic energy follows as

$$\mathcal{T}_{M_t} = \left[\frac{1}{2}\dot{\mathbf{r}}_{M_t}^T M_t \dot{\mathbf{r}}_{M_t} + \frac{1}{2}J_{yy}\dot{w}'^2\right]\Big|_{s=L} = \left[\frac{1}{2}M_t(\dot{w}+\dot{z})^2 + \frac{1}{2}J_o\dot{w}'^2\right]\Big|_{s=L} \tag{3}$$

where J_{yy} is the inertia of the proof mass about its center of gravity and $J_o = J_y y + 2M_t o_x^2$ is the rotary inertia of the proof mass that incorporates parallel axis theorem as a result of expanding $\dot{\mathbf{r}}_{M_t}^T M_t \dot{\mathbf{r}}_{M_t}$. The total kinetic energy of the harvester-mass system is found by summing equations (1) and (3).

The stored energy within the cantilever is composed of the bending potential of the brass shim and the electroelastic enthalpy of the piezoelectric laminates. Stored energy within the brass shim is presumed linear and varies in proportion to the square of the longitudinal strain

$$\mathcal{U} = \frac{1}{2}c_{xx,b}\int_{V_b} S_x^2 \,\mathrm{d}V_b \tag{4}$$

where $c_{xx,b}$ is the brass elastic modulus and S_x denotes the strain along the x-axis.

The conservative potential of the piezoceramics is expressed in terms of an electric enthalpy function. For linear piezoelectric behavior, this function consists of purely elastic and dielectric terms to describe the mechanical and electrical behaviors along with a coupling parameter that yields electromechanical effects. Mathematically, this is written in a reduced form for a beam-like device as

$$\mathcal{H} = \frac{1}{2}\int_{V_p}\left(c_{xx}^E S_x^2 - 2e_{zx}S_x E_z - \varepsilon_{zz}^S E_z^2\right)\mathrm{d}V_p \tag{5}$$

where c_{xx}^E is the elastic modulus, e_{zx} is the piezoelectric coupling coefficient, ε_{zz}^S is the dielectric constant, and E_z is the generated electric field perpendicular to the strain. However, this form is inadequate to explain empirical trends. Experimental results within the literature relating to piezoelectric plates, rods, and beams driven by weak electric fields demonstrate nonlinear effects typically characterized by frequency-dependent amplitude responses, nonlinear damping, and even bifurcation phenomena. Figure 3 shows the general trend in the voltage response normalized by the driving

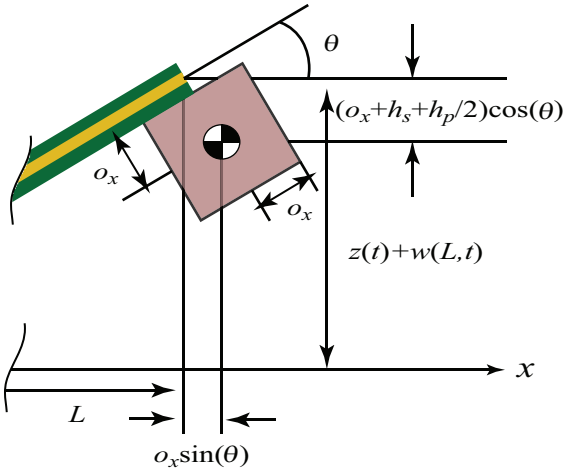

Figure 2. Closer view of the proof mass kinematics for determining the position vector from the origin to the center of mass.

amplitude for one of the experimentally identified cantilevers. All experimental tests resulted in softening frequency response curves with complicated damping characteristics. To ascertain a first principles–based model for the energy harvester, a fully nonlinear extension of equation (5) following Samal et al. (2006a) was applied that included third- and fourth-order nonlinear coupling and dielectric effects in addition to higher-order structural nonlinearities. In a similar fashion, Stanton et al. (2010a, 2010b) considered nonlinear constitutive relations for modeling piezoelectric harvesters with dielectric nonlinearities disregarded but coupling nonlinearities retained. In these studies, experimental identification using a nonlinear least squares algorithm converged upon several local minima indicating nonvanishing nonlinear coupling, although a global minimum was unattainable. In the present analysis, exhaustive simulation studies including proof mass effects revealed that numerical trends resulting from conservative nonlinear coupling and nonlinear dielectric effects were counter to the experimental measurements when a cubic structural nonlinearity was kept to explain the softening frequency response. This result is in agreement with the cubic theory of electroelasticity and reduces model complexity to that of an electromechanical Duffing oscillator with linear coupling. For high acceleration values, the inclusion of a proof mass suggested a trend indicative of higher-order structural nonlinearities (fifth- and seventh-order harmonics) along with weakened nonlinear damping effects attributable to the inertial influence of the proof mass. To model the empirical trends in this study, we employ a nonlinear electroelastic enthalpy expression that includes higher-order elastic nonlinearities up to fifth order but disregards higher-order coupling and electrical effects. Accordingly, we now have

$$\mathcal{H} = \frac{1}{2}\int_{V_p}\left(c_{xx}^{E}S_x - 2e_{zx}S_xE_z - \varepsilon_{zz}^{S}E_z^2 + \frac{2}{3}c_3S_x^3 + \frac{1}{2}c_4S_x^4 + \frac{2}{5}c_5S_x^5 + \frac{1}{3}c_6S_x^6\right)\mathrm{d}V_p \tag{6}$$

where c_3, c_4, c_5 and c_6 are nonlinear stiffness coefficients. From equation (6), the nonlinear constitutive relations are derived from the compatibility equations

$$T_x = \frac{\partial \mathcal{H}}{\partial S_x} = c_{xx}^{E}S_x - e_{zx}E_z + c_3S_x^2 + c_4S_x^3 + c_5S_x^4 + c_6S_x^6 \tag{7}$$

and

$$D_z = -\frac{\partial \mathcal{H}}{\partial E_z} = e_{zx}S_x + \varepsilon_{zz}E_Z \tag{8}$$

where T_x is the stress and D_z is the electric displacement. With this formulation the following relations hold

$$\frac{\partial^2 \mathcal{H}}{\partial S_x \partial E_z} = \frac{\partial T_x}{\partial E_z} = -\frac{\partial D_z}{\partial S_x} = \frac{\partial^2 \mathcal{H}}{\partial E_z \partial S_x} \tag{9}$$

and the necessary and sufficient thermodynamic conditions for the existence of an enthalpy function are satisfied. Due to the symmetry of the bimorph, odd nonlinearities in the enthalpy function will cancel. Thus, presuming perfect symmetry in the bimorph restricts nonlinear effects to cubic and fifth-order structural effects in the equation of motion.

The gravitational potential of the beam is also modeled for completeness and to account for induced asymmetry, although this was found to be negligible. Future investigations with heavier proof masses may induce static deformation of the beam, and the potential field for modeling is given by

$$U_g = g\left[\rho_b\int_{V_b}(w+z+o_x)\mathrm{d}x + \rho_p\int_{V_p}(w+z+o_x)\mathrm{d}x + M_tg[w(L,t)+z]\right] \tag{10}$$

where the datum is taken as the center of gravity of the proof mass, and we have again presumed small-angle rotations in determining the potential of the proof mass.

Consistent experimental observation of decreased frequency response amplitudes to higher driving amplitudes in a variety of piezoelectric cantilevers by the authors necessitates modeling nonlinear damping. In addition to conservative energy considerations, this result suggests nonvanishing virtual work contributions to the oscillatory dynamics of the beam as well. In the past, quadratic fluid damping successfully modeled this phenomena (Stanton et al., 2010a, 2010b), but the underlying physical mechanism of this influence at the scale is a relatively open question. Although air damping is a dominant source of dissipation in

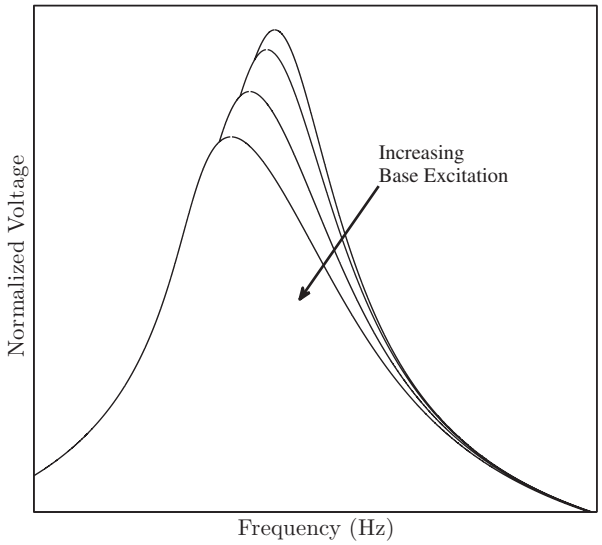

Figure 3. Illustration of the empirical trend in nonlinear resonance curves for the piezoelectric harvester. The output voltage is normalized by the drive amplitude to better portray the nonlinear response.

microcantilever systems (Zhang and Meng, 2005), the larger amplitudes in our macroscopic systems may render air damping less of a primary contributor to the dissipative influences despite the high-response velocity oscillations. In this study, we model damping that increases with the response amplitude in an alternative manner by presuming material dissipation dominates air damping. Note, however, that quadratic air damping is critical for limiting the growth of oscillations in cantilever harvesters engaging geometric and inertial nonlinearity (Daqaq et al., 2009). Considering the experimental observations within the study by Samal et al. (2006b) of nonlaminate piezoceramics, the source of nonlinear damping in this article is presumed to be due to viscoelastic effects within the piezoceramics. The brass substrate, however, experiences a virtual work in proportion to the time rate of change in strain of the form

$$\delta \mathcal{W}_b = \int_{V_p} \eta_b \dot{S}_x \delta S_x \mathrm{d}V_p \tag{11}$$

and is attributable to structural damping, losses at the clamp location, and thermoelastic dissipation, among other sources (Kamel et al., 2010).

Ikeda (1996) introduced dissipation within electroelastic media by extending the constitutive equations with time derivatives of the conservative basis variables. Later, Von Wagner (2003) employed this method to a nonlinear set of constitutive relations, and his technique is applied here. Accordingly, we extend the constitutive relations as

$$T_x = \frac{\partial \mathcal{H}}{\partial S_x} + T_{nc} \tag{12a}$$

and

$$D_z = -\frac{\partial \mathcal{H}}{\partial E_z} + D_{nc} \tag{12b}$$

where T_{nc} and D_{nc} denote nonconservative stress and electric displacement that contain both linear and nonlinear dissipative terms defined by

$$T_{nc} = \eta_p \dot{S}_x - \gamma \dot{E}_z + \zeta_a \left(\dot{S}_x^3\right) + \zeta_b \left(\dot{S}_x^5\right) \tag{13a}$$

and

$$D_{nc} = \gamma \dot{S}_x + \nu \dot{E}_z \tag{13b}$$

Thus, nonvanishing virtual work due to piezoelectric losses can be incorporated into Hamilton's extended principle through

$$\delta \mathcal{W}_p = \int_{V_p} (T_{nc} \delta S_x + D_{nc} \delta E_z) \mathrm{d}V_p \tag{14}$$

With all conservative and nonconservative energy formulations defined, we are in a position to apply variational calculus (Crandall et al., 1968) to derive the equations of motion. First, the kinetic energy (equations (1) and (3)), potential energy (equations (4) to (6) and (10)), and the virtual work (equations (11) and (14)) can be further reduced by considering a single-mode approximation of the Euler–Bernoulli strain

$$S_x = -zr(t)\phi''(x) \tag{15}$$

where $()'$ is shorthand for $\mathrm{d}/\mathrm{d}x$, $r(t)$ is the displacement, and $\phi(x)$ is the first spatial mode of a fixed-free cantilever with proof mass boundary conditions (see equations (12) and (16) within Erturk and Inman (2009a) where $J_o = I_t$). The eigenvalues and modes as within the study by DuToit et al. (2005) were also calculated with a proof-mass/cantilever overlap of o_x but were found to offer no improvement to the center of mass approximation.

The electric field can be expressed in terms of an electric potential function $\varphi(x,t)$ for the upper and lower laminates as

$$E_z^u = -\frac{\varphi'(x,t)}{h_p} \text{ and } E_z^l = \frac{\varphi'(x,t)}{h_p} \tag{16}$$

where the change in sign is due to the opposite poling directions as a consequence of a series connection between bimorph layers. Next, by defining the Lagrangian as

$$\mathcal{L} = \mathcal{T} + \mathcal{T}_{M_t} - \mathcal{H} - U_g \tag{17}$$

incorporating equations (15) and (16), and integrating over the volume of the beam, we obtain a single-mode approximation for the harvester dynamics. The variation of the Lagrangian becomes

$$\delta\mathcal{L}\approx(M\dot{r}+F_z\dot{z})\delta\dot{r}+\left(-Kr-Gr^3-Hr^6+\Theta\varphi'-F_g\right)\delta r+\left(-\tilde{\Theta}r-\tilde{C}\varphi'\right)\delta\varphi' \tag{18}$$

where the constant coefficients are defined in Appendix 1. Similarly, the virtual work is

$$\delta\mathcal{W}\approx\left[\left(D_a+D_br^2+D_cr^4\right)\dot{r}-\tilde{\Lambda}\varphi'\right]\delta r+\left[\tilde{\Lambda}\dot{r}+\chi\varphi'\right]\delta\varphi' \tag{19}$$

where linear and nonlinear structural dissipation, conversion losses, and dielectric losses are present. The electrical network introduces electronic losses across a resistive load to eliminate complications arising from voltage conditioning for a storage circuit. This improves identification of nonlinear beam parameters and serves to represent the equivalent impedance of a more complex storage network. Since the voltage is distributed across two laminate layers, we define the electric field in terms of the circuit flux linkage $\varphi=\frac{1}{2}x\dot{\lambda}(t)$ to facilitate unified variational modeling. Hamilton's extended principle for electromechanical systems is therefore

$$\int_{t_0}^{t_1}(\delta\mathcal{L}+\delta\mathcal{W}+I\delta\lambda)\mathrm{d}t=0 \tag{20}$$

where $\delta\mathcal{L}$ and $\delta\mathcal{W}$ are as before and $I\delta\lambda$ is a generalized current. For a linear resistor, this is given by

$$I\delta\lambda=\left(\frac{1}{R}\right)\dot{\lambda}\delta\lambda \tag{21}$$

where R is the load resistance. Applying the calculus of variations and collecting terms common in δr and $\delta\lambda$ yield a nonlinear equation of motion for the displacement of the cantilever

$$M\ddot{r}+\left(D_a+D_br^2+D_cr^4\right)\dot{r}+Kr+Gr^3+Hr^5-\Theta V-D_d\dot{V}=-F_g+F_z\ddot{z}(t) \tag{22}$$

and a linear equation for the harvesting circuit

$$D_e\ddot{V}+C\dot{V}+\frac{1}{R}V+\Theta\dot{r}+D_d\ddot{r}=0 \tag{23}$$

where we have also replaced the time derivative of the flux-linkage coordinate $\dot{\lambda}$ with voltage V for convenience. The form for the base acceleration $\ddot{z}(t)$ is general, but for this particular study, it is harmonic with an excitation frequency near fundamental resonance such that $\ddot{z}(t)=Z\cos\Omega_e t$, where Z is the amplitude and Ω_e is the frequency of excitation.

A dimensionless form for equations (22) and (23) may be derived by substituting a characteristic time, length, and voltage

$$T_c=\sqrt{\frac{M}{K}},\qquad L_c=\sqrt{\frac{K}{|G|}},\qquad V_c=\frac{L_c}{T_c}\sqrt{\frac{M}{C}} \tag{24}$$

into the equations of motion. Accordingly, the remainder of this article examines the following dimensionless equations for the mechanical domain

$$\ddot{x}+\left(\mu_a+\mu_bx^2+\mu_cx^4\right)\dot{x}+x-x^3+\beta x^5-\theta v-\kappa\dot{v}=-f_g+f_z\cos\Omega\tau \tag{25a}$$

and electrical domain

$$\mu_e\ddot{v}+\dot{v}+\mu_dv+\theta\dot{x}+\kappa\ddot{x}=0 \tag{25b}$$

where $x(\tau)=r(t)/L_c$, $v(\tau)=V(t)/V_c$, and the sign preceding x^3 are negative for convenience due to the softening frequency response of the beam. The dimensionless parameters are defined as

$$\mu_a=\frac{D_a}{M}\sqrt{\frac{M}{K}},\qquad \mu_b=\frac{D_b}{|G|}\sqrt{\frac{K}{M}},\qquad \mu_c=\frac{D_cK}{G^2}\sqrt{\frac{K}{M}},$$

$$\mu_d=\frac{1}{RC}\sqrt{\frac{M}{K}},\qquad \mu_e=\frac{D_d}{C}\sqrt{\frac{K}{M}},\qquad \beta=\frac{HK}{G^2}$$

$$\theta=\frac{\Theta}{\sqrt{CK}},\qquad \kappa=\frac{D_c}{MC},\qquad f_g=\frac{F_g}{K|G|}$$

and

$$f_z=F|G|Z\left(\frac{1}{K^2}\right)\sqrt{\frac{K}{|G|}}$$

while the dimensionless excitation is $\Omega=\Omega_e\sqrt{M/K}$.

Multiple time-scaling perturbation solution

This section develops an analytic solution for harvester dynamics based on perturbation methods to enable parameter identification. In particular, the method of multiple scales is employed such that a weakly nonlinear behavior can be predicted by separating the dimensionless displacement and voltage into a third-order summation of terms proportional to a small expansion parameter ε and corresponding separate time scales as

$$x(\tau)=\sum_{k=0}^{1}\varepsilon^kx_k(T_0,T_1)\quad\text{and}\quad v(\tau)=\sum_{k=0}^{1}\varepsilon^kv_k(T_0,T_1) \tag{26}$$

and time derivative operators become

$$\frac{\mathrm{d}}{\mathrm{d}\tau} = \frac{\partial}{\partial T_0} + \varepsilon \frac{\partial}{\partial T_1} + \mathcal{O}(\varepsilon^2) \tag{27}$$

and

$$\frac{\mathrm{d}^2}{\mathrm{d}\tau^2} = \frac{\partial^2}{\partial T_0^2} + 2\varepsilon \frac{\partial^2}{\partial T_0 \partial T_1} + \mathcal{O}(\varepsilon^2) \tag{28}$$

Following Masana and Daqaq (2011), we order the coupling parameter θ in the mechanical dynamics to appear at higher-order perturbation corrections but to an order of zero in the electrical network. This allows for the electrical circuit to be studied as a driven linear system in terms of the zeroth-order perturbation correction for displacement. We also balance all damping, nonlinear stiffness terms, and harmonic forcing to appear at the first-order correction. The constant force due to gravity is ordered to $\mathcal{O}(1)$, so that these effects are not lost in the perturbation solution. Furthermore, extensive simulation trials indicated that for the voltages and strains induced in our experimental devices, the terms encompassing dissipative coupling and dielectric losses were negligible. Hence, we choose to order these terms such that the derived solvability condition does not reflect these influences. As a result, our focus is now on the following system of equations:

$$\begin{aligned} \ddot{x} + x + f_g = & -\varepsilon\big[\left(\mu_a + \mu_b x^2 + \mu_c x^4\right)\dot{x} \\ & -x^3 + \beta x^5 + \theta v - f_b \cos \Omega\tau\big] + \varepsilon^2 \mu_c \dot{v} \end{aligned} \tag{29a}$$

and

$$\dot{v} + \mu_e v = -\theta\dot{x} - \varepsilon(\mu_e \ddot{v} + \mu_c \ddot{x}) \tag{29b}$$

where ε serves as a bookkeeping parameter that will be set to unity at the end of our analysis. Multiple time-scaling perturbation solution requires the excitation frequency Ω to instead be expressed in terms of the nearness to the unit resonance by

$$\Omega = 1 + \varepsilon\sigma \tag{30}$$

where $\varepsilon\sigma$ is a small detuning away from resonance. Substituting equation (26) into equations (29a) to (29b) and collecting terms independent of ε gives

$$D_1^2 x_0 + x_0 = -f_g \tag{31a}$$

and

$$D_1 v_0 + \mu_d v_0 = -\theta D_0 x_0 \tag{31b}$$

where D_k^n denotes the nth partial derivative with respect to the kth time scale (i.e. $D_k^n = \partial T_k^n / \partial T_k^n$). Solving for x_0 yields simple harmonic motion offset by f_g for the displacement, while the voltage equation yields a forced response due to x_0 with an exponential decay. Hence, in steady state, we have solutions for the lowest order contributions

$$x_0 = A(T_1)e^{jT_0} - f_g + \text{c.c.} \tag{32a}$$

and

$$v_0 = -\left(\frac{j}{j + \mu_e}\right)\theta A(T_1)e^{jT_0} + \text{c.c.} \tag{32b}$$

where $j = \sqrt{-1}$, $A(T_1)$ is a complex amplitude in the slower time scale and c.c. indicates a complex conjugate. Substituting the order zero solution into the equations at first order in ε gives the first perturbation correction

$$\begin{aligned} D_0^2 x_1 + x_1 = & -\big[2D_0 D_1 x_0 + \left(\mu_a + \mu_b x_0^2 + \mu_c x^4\right) D_0 x_0 \\ & -x_0^3 + \beta x_0^5 - \theta v_0 + f_z \cos(T_0 + \sigma T_1)\big] \end{aligned} \tag{33}$$

Upon consideration of the zeroth-order perturbation corrections to the displacement and voltage (equations (32a) and (32b)) in equation (33), the solvability condition is derived by disregarding higher harmonics and setting secular terms to zero. Hence, we have

$$\begin{aligned} 0 = & (P_r - jP_i)A + (Q_r - jQ_i)A^2\bar{A} \\ & -(S_r + jS_i)A^3\bar{A}^2 - 2jA' - \frac{1}{2}f_z e^{j\sigma T_1} \end{aligned} \tag{34}$$

where the over bar denotes a complex conjugate, $()'$ now represents a derivative with respect to the slower time scale T_1, and the model parameters are collected as

$$P_r = f_g^2\left(3 - 5\beta f_g^2\right) - \frac{\theta^2}{1 + \mu_d^2} \tag{35}$$

$$P_i = \mu_a + \mu_b f_g^2 + \mu_c f_g^4 + \frac{\mu_d \theta^2}{1 + \mu_d^2} \tag{36}$$

$$Q_r = 3 - 30\beta f_g^2 \tag{37}$$

$$Q_i = \mu_b + 6\mu_c f_g^2 \tag{38}$$

$$S_r = 10\beta \tag{39}$$

and

$$S_i = 2\mu_c \tag{40}$$

Substituting a polar expression for the complex amplitude

$$A = \frac{1}{2}ae^{j\psi} \tag{41}$$

where a and ψ indicate a real-valued amplitude and phase, respectively, and separating the right-hand side of equation (34) into real and imaginary components gives

$$a\psi' = -\frac{1}{2}P_r a - \frac{1}{8}Q_r a^3 + \frac{1}{32}S_r a^5 + \frac{1}{2}f_z \cos(\sigma T_1 - \psi) \tag{42a}$$

and

$$a' = -\frac{1}{2}P_i a - \frac{1}{8}Q_i a^3 - \frac{1}{32}S_i a^5 - \frac{1}{2}f_z \sin(\sigma T_1 - \psi) \tag{42b}$$

Transformation to an autonomous system is achieved by letting $\phi = \sigma T_1 - \psi$, and the steady-state frequency response curve is derived by setting all time derivatives in the system above to zero. Accordingly, steady-state solutions obey the algebraic system

$$f_z \cos\phi = (2\sigma + P_r)a + \frac{1}{4}Q_r a^3 - \frac{1}{16}S_r a^5 \tag{43a}$$

$$-f_z \sin\phi = P_i a + \frac{1}{4}Q_i a^3 + \frac{1}{16}S_i a^5 \tag{43b}$$

where the phase can be eliminated by squaring and adding both equations. The steady-state magnitude and phase are therefore

$$a^2 = \frac{f_z^2}{\left(2\sigma + P_r + \frac{1}{4}Q_r a^2 - \frac{1}{8}S_r a^4\right)^2 + \left(P_i + \frac{1}{4}Q_i a^2 + \frac{1}{8}S_i a^4\right)^2} \tag{44}$$

and

$$\tan\phi = \frac{P_i + \frac{1}{4}Q_i a^2 + \frac{1}{8}S_i a^4}{2\sigma + P_r + \frac{1}{4}Q_r a^2 - \frac{1}{8}S_r a^4} \tag{45}$$

Alternatively, one can solve for the frequency detuning as

$$\sigma = -\frac{1}{2}P_r - \frac{1}{8}Q_r a^2 + \frac{1}{16}S_r a^4 \pm \left[\frac{f_z^2}{a^2} - \left(P_i + \frac{1}{4}Q_i a^2 + \frac{1}{8}S_i a^4\right)^2\right]^{1/2} \tag{46}$$

The harvester's nonlinear resonance has several interesting features in comparison to a classic Duffing oscillator. First, as a coupled electromechanical system, the system resonant frequency is shifted a value P_r away from the purely mechanical cantilever resonance. In view of equation (35), a linear harvester is shifted $(\theta^2/1 + \mu_d^2)$ as the energy transfers through θ between the electrical and mechanical domains. By considering a static gravitational load, it is also not surprising that consideration of this preload also shifts resonance away from that predicted by Euler–Bernoulli beam theory. Second, the linear dissipation term P_i is augmented by the electrical dissipation through the dimensionless load μ_d. Including fifth order, structural effects are captured through the term S_r, and third- and fifth-order dissipation appears within Q_i and S_i, respectively. The manifestation of these results in the mathematics is in harmony with current experimental studies and those within the literature (Stanton et al., 2010a, 2010b).

Although equation (44) is tenth order in a, only few solutions will have no imaginary component and are hence physically meaningful. With only a cubic nonlinearity, the existence of three solutions is a harbinger of a saddle node bifurcation and jump phenomena in the harvester response. Because our experimental trials did not indicate jump phenomena would occur for the range of drive amplitudes studied, we complete our perturbation analysis and forgo a discussion on linear stability of the steady-state motion. Despite the fifth-order nonlinearity, determining the stability of steady-state motion may be accomplished by straightforward extension of methods for typical Duffing oscillators. While the study by Nayfeh and Mook (1979), among many others, details procedures for doing so, a good stability analysis and discussion in the context of a nonlinear harvester can be found in a recent article by Daqaq et al. (2009).

Experimental investigation and identification

This section describes the series of experiments that were conducted to assess the validity of the proposed model and to enable parameter identification. Two bimorph cantilevers, one symmetrically laminated with PZT-5H and another with PZT-5A (model numbers T226-H4-203X and T226-A4-203X, respectively, and manufactured by Piezo Systems Inc.), were separately investigated. However, comparative analysis was facilitated by affixing each bimorph to a clamp with similar overhang lengths and proof masses and across the same electrical impedance load. A picture of a typical experiment is shown in Figure 4. Base motion was recorded by an accelerometer (PCB Piezotronics U352C67), and the cantilever's transverse tip velocity relative to the fixed reference frame is measured using a laser vibrometer (Polytec OFV353 laser head with OFV3001 vibrometer). The cantilevers were never unclamped during the course of the experimental investigation and remained secured to the clamping apparatus as shown in Figure 4, while successive proof masses were affixed. Table 1 lists the plane-stress elastic, piezoelectric, and dielectric properties of each beam, as well as the proof mass properties. The dimensionless mass ratios

$$\alpha = \frac{M_t}{mL} \tag{47}$$

where $m = b(\rho_s h_s + 2\rho_p h_p)$ is the mass per unit length of the cantilever. The values of m in the experiments were 0, 0.298, and 0.976 for PZT-5H and 0, 0.293, and 0.972 for PZT-5A. In all, 6 different cantilever configurations

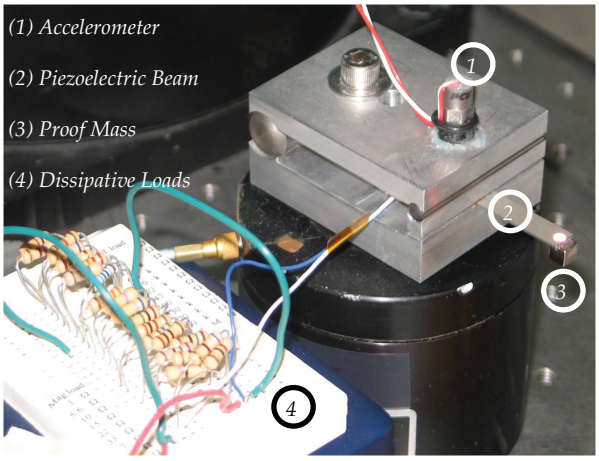

Figure 4. Experimental setup for all six test configurations.

were tested over 5 distinct frequencies and for 11 different base excitation values for PZT-5H and 9 base excitation values for PZT-5A.

Isolating the source of nonlinearity to piezoelectric effects was paramount in designing the experiment. Hence, electrical impedance due to a resistive load in the electronics was utilized so as not to invigorate higher-order harmonics stemming from nonlinear AC to DC electronic conversion or switching techniques. In all experiments, $R = 100$ Kohm. Also, the cantilever dimensions were selected such that ensuing small amplitude oscillations despite large drive amplitudes ensures the validity of linear Euler–Bernoulli beam theory. In other words, no geometric nonlinearities such as nonlinear inertia or third-order structural nonlinearity (which is hardening in the first vibration mode of a cantilever) interfere with the already nonlinear cantilever response.

Linear domain frequency response functions were first measured for each case to identify resonance and linear damping parameters. Linear damping is presumed proportional to the cantilever resonance such that $D_a = 2\zeta\omega_n$, where ζ is a dimensionless damping factor and ω_n is the uncoupled fundamental frequency of the beam. Afterward, highly sampled (50 kHz) steady-state oscillations near resonance were recorded for increasing levels of base excitation. The frequency content of the data was analyzed via a power spectral density (PSD) function (in MATLAB), and the magnitude of the harmonics was found by Parseval's theorem as

$$X = \left[2 \int_{\omega_a}^{\omega_b} P_X(\omega) \mathrm{d}\omega \right]^{1/2} \tag{48}$$

where X is the signal amplitude, P_X is the PSD, and ω is the frequency. The magnitude of the acceleration, tip velocity, and voltage signals at the first excitation frequency was observed to be of the orders of magnitude greater than odd integer multiples of the same frequency as expected, and reconstruction of the time series signal was coincident with the recorded time series for all driving amplitudes. Hence, a single-mode approximation is indeed sufficient to model the dynamics of the harvester. Average base acceleration levels for the PZT-5H cantilever (with and without a proof mass) were 60 mg, 145 mg, 230 mg, 310 mg, 430 mg, 560 mg, 840 mg, 1.12g, 1.4g, 1.7g, and 2g, while the PZT-5A cantilever was excited at 50 mg, 100 mg, 200 mg, 300 mg, 400 mg, 800 mg, 1.2g, 1.6g, and 2g.

The nonlinear resonance curve given by equation (46) is used in conjunction with experimental data to fit parameters in accordance with a nonlinear least squares optimization algorithm. This has been previously done in the study by Stanton et al. (2010a, 2010b), and we again stress the importance of simultaneously studying the response in both the mechanical and electrical domains when exploring the variety of local minima such an algorithm may converge upon. Good experimental data fitting in the voltage domain does not imply success in matching the displacement amplitude. For example, in the course of the present investigation, a fully nonlinear enthalpy function was studied with up to fourth-order electromechanical and dielectric effects. Initially, it was found that higher-order electromechanical coupling proportional to $S_x^2 E_x^2$ generated excellent agreement in the voltage domain only to be negated by extremely suppressed displacement curves. Hence, all optimization routines were examined for agreement in both voltage and mechanical response. After a wide range of analytical and numerical investigation spanning all the possible nonlinearities, it was found that with the new nonlinear structural damping model, parameter identification with conservative

Table 1. Geometric and material properties of the bimorph cantilevers.

Parameter	PZT-5H beam	PZT-5A beam
Length (L) (mm)	24.06	23.82
Width (b) (mm)	6.4	6.4
Brass thickness (h_b) (mm)	0.140	0.140
Brass mass density (ρ_b) (kg/m^3)	9000	9000
Brass elastic modulus ($c_{xx,b}$) (GPa)	105	105
PZT layer thickness (h_p) (mm)	0.265 (each)	0.265 (each)
PZT mass density (ρ_p) (kg/m^3)	7500	7750
PZT elastic modulus (c_{xx}^p) (GPa)	60.6	61
Piezoelectric constant (e_{zx}) (C/m^2)	−16.1	−10.1
Permittivity constant ($\bar{\varepsilon}_{zz}^s$) (nF/m)	25.55	13.27
Mass 1 total mass (M_t) (kg)	0.24	0.24
Mass 2 total mass (M_t) (kg)	0.787	0.795
Mass 1 side length ($2o_x$) (mm)	3.2	3.2
Mass 2 side length ($2o_x$) (mm)	4.7	4.7
Mass 1 rotary inertia (J_o) (kg m^2)	1.2903×10^{-9}	1.2903×10^{-9}
Mass 2 rotary inertia (J_o) (kg m^2)	8.7386×10^{-9}	8.6549×10^{-9}

nonlinearities due to elasticity alone was sufficient to achieve good experimental fits. This is plausible in view of the weak electric field generation (at most 25–30 V/mm). Weak fields of similar magnitudes examined in several studies concerning piezoceramics for ultrasonic motor applications (Parashar and Von Wagner, 2004; Samal et al., 2006b) have also not been strong enough to evoke nonlinear coupling and dielectric effects but maintain strong elastic and damping nonlinearity.

Figure 5 shows the strong model agreement for cantilever beams with no attached proof mass. Proper parameter identification is assured given the theoretical agreement in both the voltage response and tip displacement. Each graph presents several nonlinear resonance curves to demonstrate the softening and nonlinear damping trends. Figure 5(a) and (c) displays the results for PZT-5H, and Figure 5(b) and (d) displays the results for PZT-5A. To highlight the importance of nonlinear modeling, the frequency response functions for the linear model are also shown. Both cantilevers begin to exhibit nonlinear resonance curves beyond $Z \approx 0.6g$, a point beyond which the nonlinear damping and elasticity conspire to shift and limit the frequency response well away from that predicted by a linear model. With the nonconservative modeling, parameter identification yields a larger fourth-order elasticity coefficient for both PZT-5H and PZT-5A than the values reported in prior studies employing a nonlinear air drag model (Stanton et al., 2010a, 2010b). However, in keeping with previous results, PZT-5A is verified to maintain a larger softening effect in comparison to PZT-5H, as indicated by the larger value for c_4 in Table 2. For the full range of experimental tests, modeling cubic nonlinearities due to x^3 and $\mu_b x^2 \dot{x}$ were found to be sufficient for both cantilevers with subtle deviation near $Z = 2g$. Accordingly, with no proof mass, a nonlinearly damped Duffing oscillator is accurate for a large range of base acceleration levels. The section titled "Linear versus nonlinear modeling" provides a quantitative approach for determining the accuracy of the nonlinear model.

With the addition of a proof mass, higher-order nonlinearities begin to influence the harvester motion. In fact, in their analysis of a piezoelectric shell, Samal et al. (2006b) noted a likely need for damping terms larger than third order. While our derivation included fifth-order damping and elasticity, it was determined that disregarding seventh-order nonlinearities began to reduce the model accuracy for the highest acceleration levels and the largest proof mass. Considering realistic applications are not likely to experience such large acceleration drives, we instead focus on the results for which the fifth-order model retains validity. Figure 6 gives the results for the PZT-5H beam for two proof masses and the same five base acceleration levels. The increased inertia in the second proof mass case generates a larger amplitude motion and hence higher voltages in comparison to the first proof mass. The nonlinear resonance curves coincident with the experimental data include terms identified proportional to β and μ_c. Overlayed on the same plot are nonlinear resonance curves for the model with $\beta = \mu_c = 0$. For $Z > 1g$, the resonance curves begin to shift to the right and the cubic model breaks down. This is especially true when α is closer to unity. The increased inertia also assuages the severity of the third-order damping that was so strong in the no-proof-mass case. This is modeled as amplitude-dependent damping through a higher-order term proportional to μ_c. The fifth-order influences are expounded for the PZT-5A cantilever, which already experiences a stronger third-order nonlinearity. Figure 7 mirrors the third-order to fifth-order model comparison but for a different set of excitation values. This is because for $\alpha = 0.972$ and $Z > 1.2g$, we found that the data could only be well characterized by a more complex seventh-order dynamical system. Again, due to the continued low electric field generation, simulation results encompassing nonlinear coupling, dielectric losses, and electromechanical losses could not adequately match the empirical trends. Hence, seventh-order and higher harmonics in the frequency analysis of the time series data are suspected to also be due to material elasticity. The threshold for which the cubic model breakdown occurs with the inclusion of a proof mass for PZT-5A is lower in comparison to PZT-5H. Figure 7(b) indicates that the cubic model has a much more limited range of validity as α increases. Symmetry breaking and longitudinal stretching due to the tip mass orientation is not suspected as a cause for the breakdown of the fifth-order model. Quadratic nonlinearities would only further soften the response (Nayfeh and Mook, 1979), which is counter to the empirical results, and the heaviest proof mass did not induce initial curvature or a strong zeroth harmonic in the experimental time series. However, nonideal clamp conditions could also induce the increasing shift back toward linear resonance by generating a potential function with a weak dead-zone nonlinearity. To rule out hardening due to geometric effects, the equations of motion were rederived with nonlinear Euler–Bernoulli beam theory only to find that the nonlinear strain assumption introduced nonlinear terms of an order of magnitude too small to be of any consequence.

One issue that arose in the course of this investigation, even for the highly linear oscillations, is that nonlinear damping parameters were not global and are moderately influenced by the addition of a proof mass. The best-fit dimensionless mechanical damping constants for all cases are listed in Table 3. While proof masses are known to require modification of linear damping parameters, a more systematic approach for determining nonlinear damping in piezoelectric energy harvesters is a topic for further research in the future.

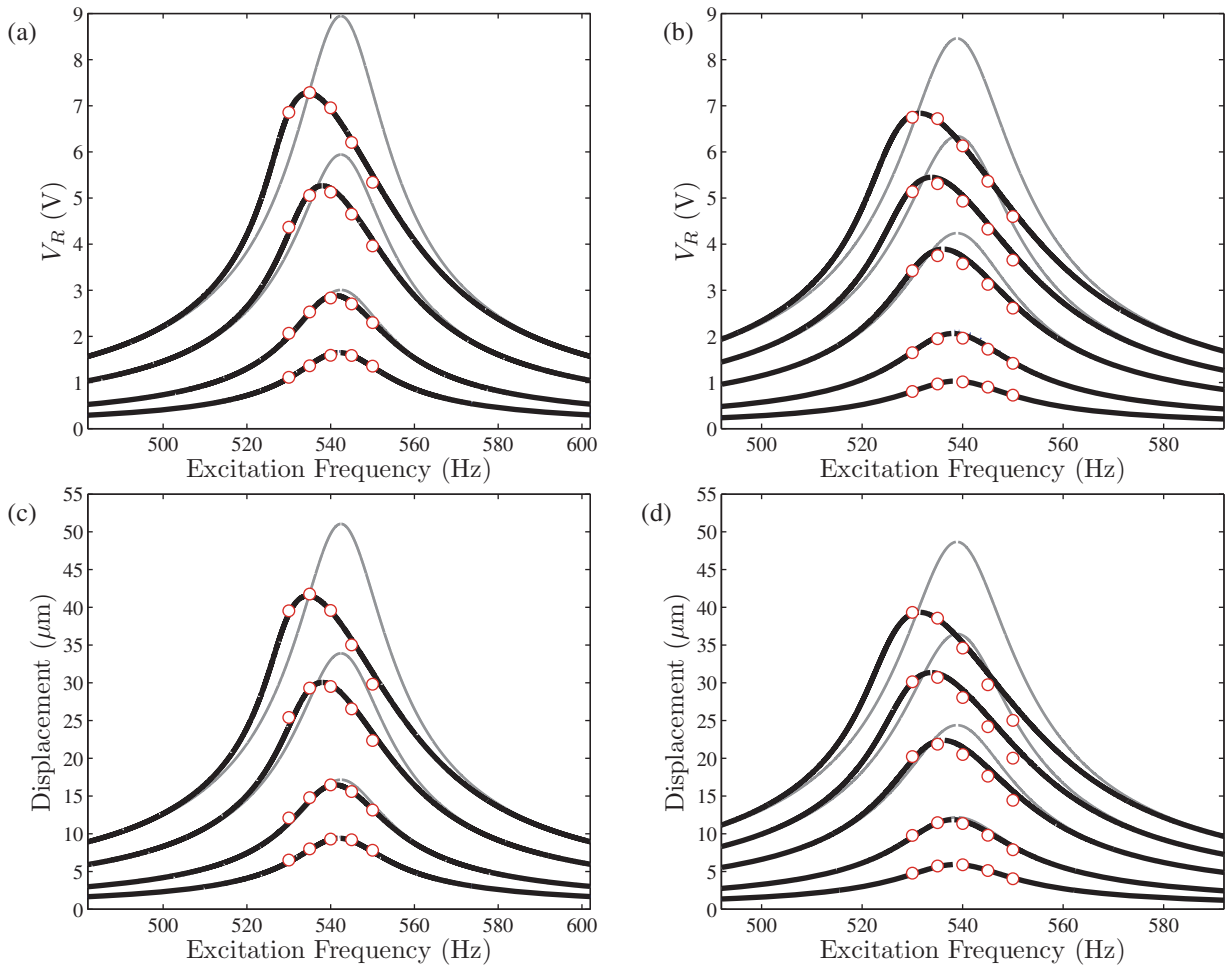

Figure 5. Experimental data points (circles), identified nonlinear resonance curves (black lines), and the linear model predictions (gray lines) for (a and c) PZT-5H and (b and d) PZT-5A bimorph with no attached proof mass. The excitation levels shown for PZT-5H are 0.3 g, 0.56 g, 1.12 g, and 1.6 g, and for PZT-5A, the excitation levels are 0.2 g, 0.4 g, 0.8 g, 1.2 g, and 1.6 g.

Table 2. Identified higher-order elasticity coefficients for PZT-5H and PZT-5A.

	PZT-5H	PZT-5A
c_4	-9.6086×10^{17}	-9.7727×10^{17}
c_6	9.6950×10^{25}	1.4700×10^{26}

This would be in the same vein as the damping analysis in the study by Kim et al. (2010).

Linear versus nonlinear modeling

Guidelines for which simpler linear modeling is sufficient before nonlinear effects can no longer be ignored are desirable. Hence, this section develops a quantitative metric for which application of a nonlinear model is more appropriate for predicting harvester performance. The approach suggested herein studies the contributions of the lowest order nonlinear terms in the perturbation solution, which in this case are cubic, to determine a point for which seeking a simple linear model becomes a poor choice. We choose to disregard the influence of gravity, provided the lack of induced curvature wrought by the addition of a proof mass, and to eliminate coupling terms in the perturbation solution. Accordingly, we begin by estimating the condition for which the third-order nonlinearities will be of the same order as the linear terms. In view of equations (42a) and (42b), this occurs when

$$\frac{1}{2}|P_r|a = \frac{1}{8}|Q_r|a^3 \tag{49}$$

which translates to a critical dimensionless displacement a_0 and voltage v_0 defined by

$$a_0^2 = 4\left|\frac{P_r}{Q_r}\right| \tag{50a}$$

and

$$v_0^2 = 4\left(\frac{\theta^2}{1+\mu_d}\right)\left|\frac{P_r}{Q_r}\right| \tag{50b}$$

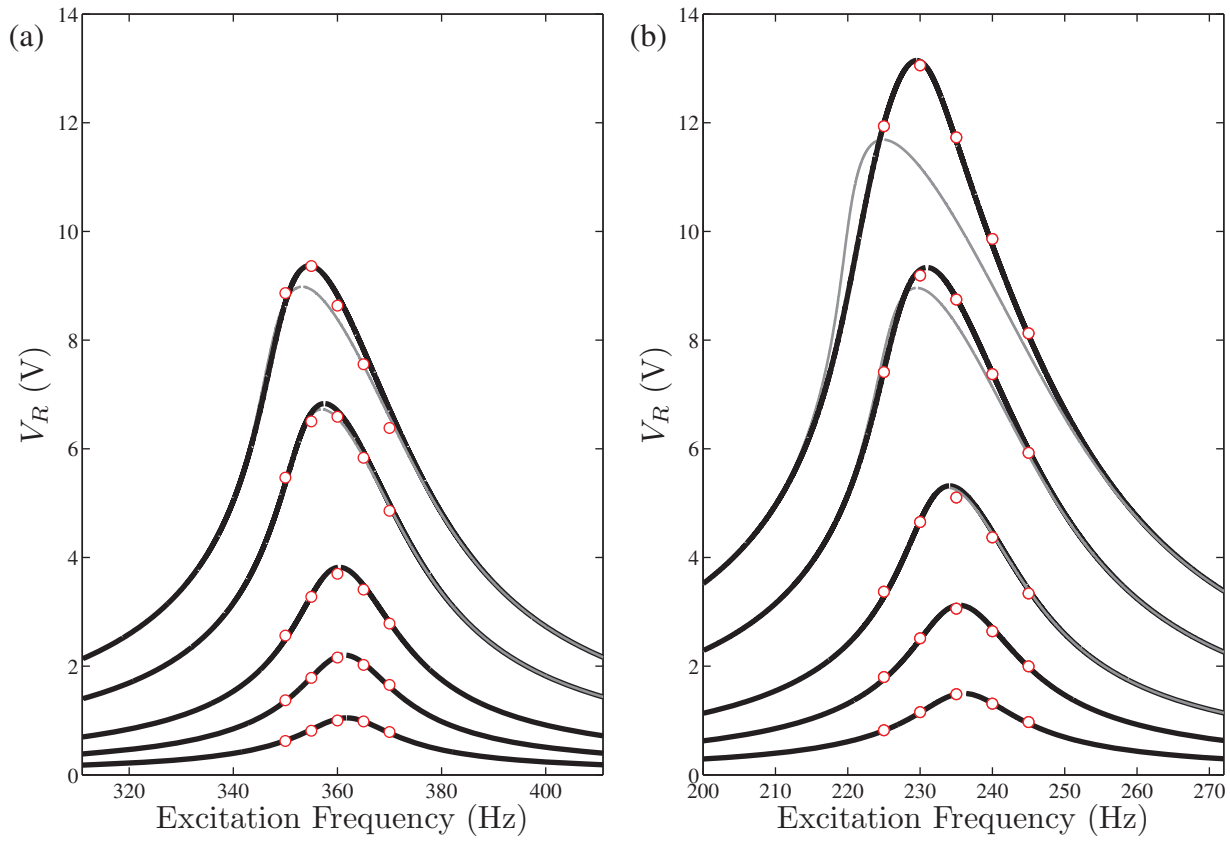

Figure 6. Experimental data points (circles), identified nonlinear resonance curves with fifth-order nonlinearities (black lines), and the cubic model predictions (gray lines) for the PZT-5H bimorph with (a) $M_t = 0.24$ kg and (b) $M_t = 0.787$ kg. The excitation levels shown are 0.145 g, 0.31 g, 0.56 g, 1.12 g, and 1.7 g.

For PZT-5H, with no proof mass excited near resonance ($\Omega_e = 540$ Hz), solving equation (50a) gives $a_0 = 0.3199$ and equation (50b) yields $v_0 = 0.0887$. However, as shown in Figure 8, this value is well above the point from which the more accurate nonlinear solution begins to deviate from the linear solution. This means that while the nonlinear and linear terms are not of the same order, nonlinear effects can still be invigorated before a_0, and hence, v_0 reaches the critical value.

The next step toward guiding application of the nonlinear nonconservative model is to define a suitable measure for which the linear model's overprediction becomes unacceptable. Since the generated power is of primary importance in evaluating a harvester's performance, we calculated the error in generated power between the linear and nonlinear models according to

$$\mathcal{E}_P = \frac{|P_{\text{lin}} - P_{\text{nonlin}}|}{P_{\text{lin}}} \tag{51}$$

where P_{lin} and P_{nonlin} denote the dimensional power dissipated by the resistive load. Figure 9 gives the trend in percent error between the linear and fully nonlinear models for the PZT-5H beam with no proof mass as a function of the dimensionless drive and at the same driving frequency as before (540 Hz). The 10% and 20% error thresholds are crossed when $f_z = 0.0054$ and $f_z = 0.0074$, respectively. The corresponding nonlinear amplitude response as calculated from equation (44) indicates that a minimum 10% error in generated power occurs for $a_0^{\text{crit}} \geq 0.123$ and $v_0^{\text{crit}} \geq 0.034$, while a minimum 20% error occurs for $a_0^{\text{crit}} \geq 0.159$ and $v_0^{\text{crit}} \geq 0.044$. Considering the conditions for which both linear and nonlinear terms in the multiple scales modulation equations were of the same order (equations (50a) and (50b)), the 10% error threshold is approximately crossed when

$$a_{5\text{H},10}^{\text{crit}} \approx \frac{3}{4}\left(\left|\frac{P_r}{Q_r}\right|\right)^{1/2} \text{ and } v_{5\text{H},10}^{\text{crit}} \approx \frac{3}{4}\left(\frac{\theta}{\sqrt{1+\mu_d}}\right)\left(\left|\frac{P_r}{Q_r}\right|\right)^{1/2} \tag{52a}$$

while the 20% error threshold is given by

$$a_{5\text{H},20}^{\text{crit}} \approx \left(\left|\frac{P_r}{Q_r}\right|\right)^{1/2} \text{ and } v_{5\text{H},20}^{\text{crit}} \approx \left(\frac{\theta}{\sqrt{1+\mu_d}}\right)\left(\left|\frac{P_r}{Q_r}\right|\right)^{1/2} \tag{52b}$$

Figure 10 verifies an expectation that lower excitation thresholds will accumulate larger error due to the stronger softening effect of PZT-5A. Using the same

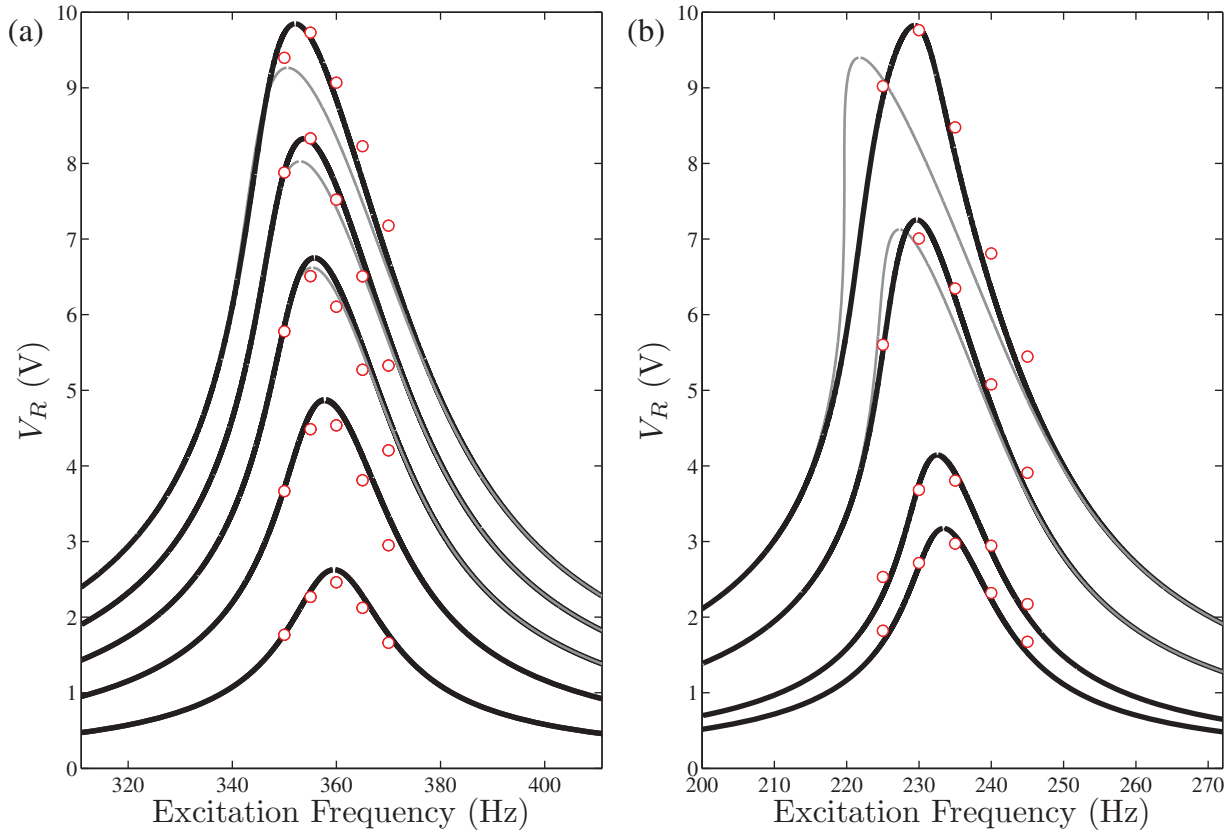

Figure 7. Experimental data points (circles), identified nonlinear resonance curves with fifth-order nonlinearities (black lines), and the cubic model predictions (gray lines) for the PZT-5A bimorph with (a) $M_t = 0.24$ kg and (b) $M_t = 0.795$ kg. The excitation levels in (a) are 0.4 g, 0.8 g, 1.2 g, 1.6 g, and 2 g, while in (b), we show 0.3 g, 0.4 g, 0.8 g, and 1.2 g.

Table 3. Identified dimensionless damping parameters for all six cantilever configurations.

Cantilever configuration	μ_a	μ_b	μ_c
PZT-5H, no proof mass	0.0086	0.895	−2.3
PZT-5H, proof mass 1	0.0052	1.149	−3.5
PZT-5H, proof mass 2	0.008	0.977	−2.7
PZT-5A, no proof mass	0.0088	1.021	0
PZT-5A, proof mass 1	0.0114	0.893	0
PZT-5A, proof mass 2	0.0125	0.453	0.1

reasoning for a mathematical development as before, we find that for PZT-5A, the 10% error threshold is approximately crossed when

$$a^{\text{crit}}_{5A,\,10} \approx \frac{2}{3}\left(\left|\frac{P_r}{Q_r}\right|\right)^{1/2} \text{ and } v^{\text{crit}}_{5A,\,10} \approx \frac{2}{3}\left(\frac{\theta}{\sqrt{1+\mu_d}}\right)\left(\left|\frac{P_r}{Q_r}\right|\right)^{1/2} \tag{53a}$$

while the 20% error threshold, similar to that for PZT-5H, is found to also be scaled by one

$$a^{\text{crit}}_{5A,\,20} \approx \left(\left|\frac{P_r}{Q_r}\right|\right)^{1/2} \text{ and } v^{\text{crit}}_{5A,\,20} \approx \left(\frac{\theta}{\sqrt{1+\mu_d}}\right)\left(\left|\frac{P_r}{Q_r}\right|\right)^{1/2} \tag{53b}$$

The addition of a proof mass changes the above guidelines. For example, the scaling factor for the 10% error threshold for the PZT-5A beam with the heaviest proof mass was found to be about 6/5 as opposed to 2/3 for the no-proof-mass case. Similarly, the second

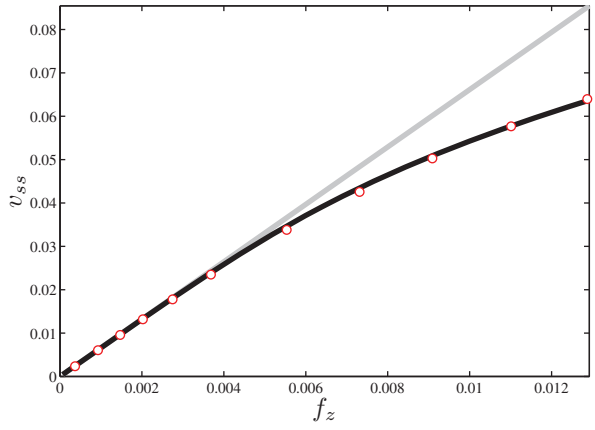

Figure 8. Experimental data points (red circles), nonlinear prediction (black line), and linear theory (gray line) for the voltage response at $\Omega = 540$ Hz for the PZT-5H bimorph with no proof mass.

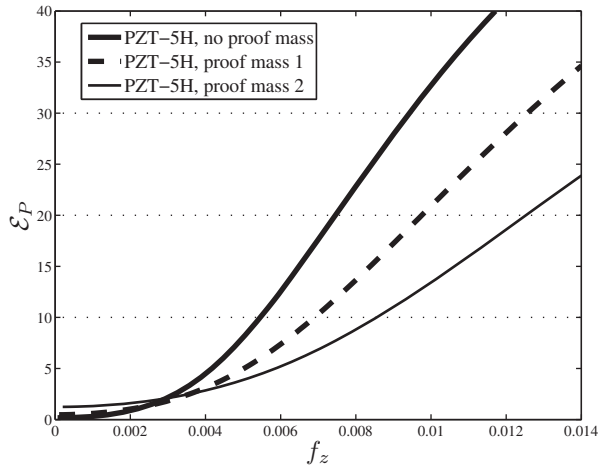

Figure 9. Error in predicted power due to linear piezoelectricity assumptions for the PZT-5H bimorph.

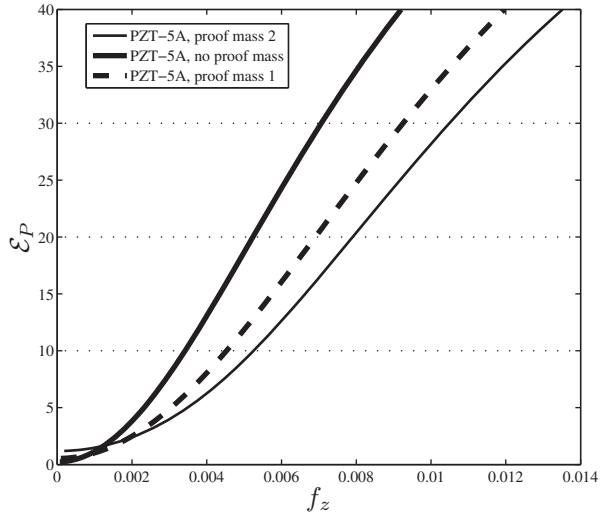

Figure 10. Error in predicted power due to linear piezoelectricity assumptions for the PZT-5A bimorph.

proof mass attached to the PZT-5H results in 10% error for a scaling factor of 9/10 instead of 3/4 for the no-proof-mass case. This further supports the experimental and theoretical findings that a proof mass can have a strong influence on the ensuing nonlinear response of a piezoelectric beam. As may also be expected, the change in scaling factor for PZT-5A is far greater than for PZT-5H due to the larger material softness.

To better visualize the influence of a proof mass on the nonlinear dynamics, Figures 11 and 12 show how both the base acceleration and proof mass influence the error in generated power from the linear model. In both graphs, there is an approximately linear relationship between the harvester-mass ratio and base acceleration and the resulting linear model error in generated power. Figures 11 and 12 also show the significantly stronger nonlinear response characteristics of PZT-5A, where the error thresholds between the more accurate nonlinear model and the standard linear model are much lower in comparison to PZT-5H.

These figures are of particular value for defining parameter regions for which a linear model is sufficient or when nonlinear modeling is more appropriate. For $\mathcal{E}_P \leqslant 10\%$, a linear model will provide a simple determination of the harvester response and is thus adequate. Depending on one's willingness to accept increasing error, the appropriateness of a linear approach will vary. For a PZT-5H cantilever with no proof mass, a linear model will be sufficient up to about $Z = 0.8\,g$, whereas a linear model for the same cantilever consisted of PZT-5A will become unsatisfactory when $Z = 0.5\,g$. In all cases, successively heavier proof masses introduce piezoelectric nonlinearity and greatly reduce the parameter space for which the validity of a linear model is an acceptable modeling assumption. The linear relationships were determined by a regression analysis and are of the form

$$Z = p_1\alpha + p_0 \tag{54}$$

where α is the mass ratio from equation (47) and Z is the base acceleration. Numerical parameters for p_1 and p_0 are listed in Tables 4 and 5. For a given base acceleration Z, mass ratio α, and error tolerance $\mathcal{E}_P$, the regression lines provide a guide for which linear piezoelectric constitutive relations will accurately model the harvester response.

Summary and conclusions

This article thoroughly investigated the influence of two types of common piezoelectric materials on the response of prototypical energy-harvesting beams. The devices were excited from low to high g base acceleration and for two different proof masses. Nonlinear resonance curves were observed and modeled from the first principles with a dissipation formulation due to viscoelectroelasticity. The Rayleigh–Ritz method was employed to directly derive a system of ordinary differential equations through Hamilton's extended principle. The dynamical system was solved analytically by the method of multiple scales, and the ensuing nonlinear frequency response function was used to provide a basis for parameter identification in conjunction with steady-state laboratory measurements. Following the analysis of description of the experiment and findings, a framework for determining when nonlinear modeling becomes necessary was provided.

Several important observations and conclusions are summarized as follows:

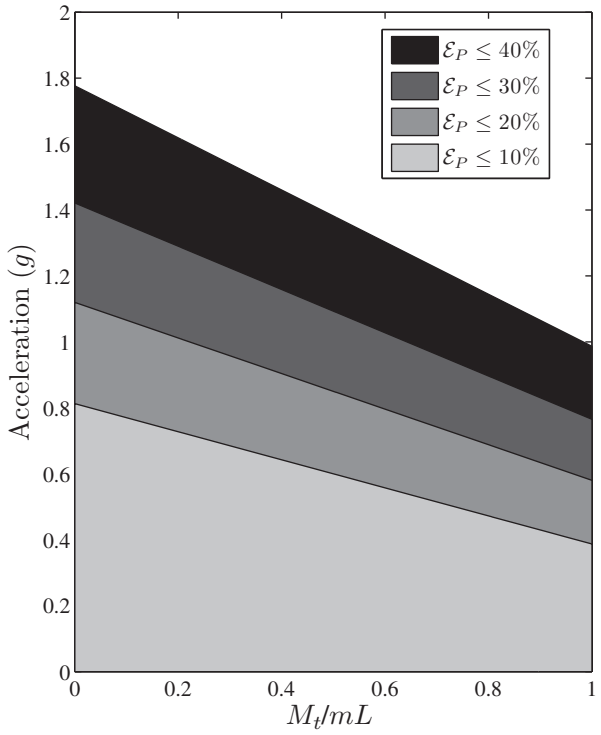

Figure 11. Influence of the mass ratio α and base acceleration on the linear model error for the predicted power of the PZT-5H bimorph.

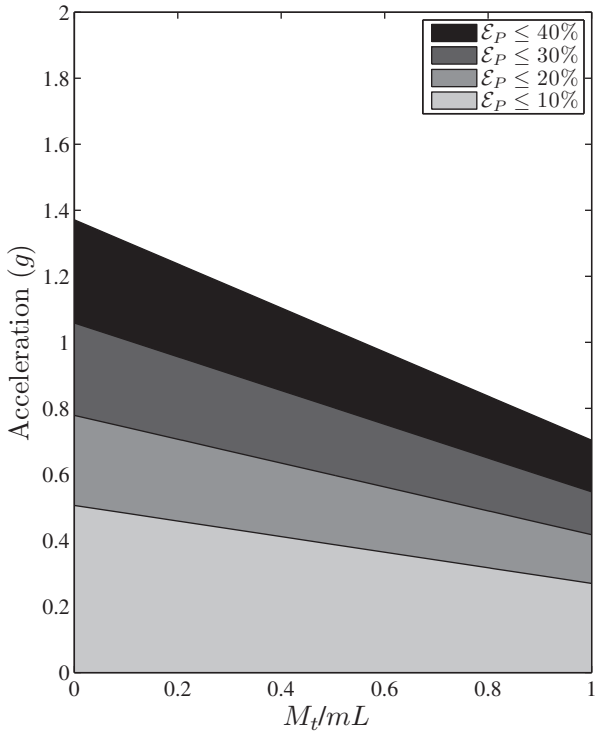

Figure 12. Influence of the mass ratio α and base acceleration on the linear model error for the predicted power of the PZT-5A bimorph.

1. From a kinematic perspective, linear Euler–Bernoulli beam theory is appropriate for our experiments and for a wide range of bimorph harvesters, especially if uniformly laminated. A third-order strain assumption along with an inextensibility condition (Da Silva and Glynn, 1978; Stanton and Mann) was modeled only to find that geometric nonlinearities were too small to have any influence.
2. Nonlinear damping is critical and can be well explained and modeled by nonconservative piezoelectric constitutive relations. However, more research is required to determine the interplay between material losses and fluid-structure interaction. This is an important undertaking in view of the fact that nonlinear damping was observed to be reducing the response amplitude at resonance *before* cubic nonlinearities begin to shift the resonance curves to the left.
3. Elasticity is the primary source of nonlinearity. That is, higher-order coupling and dielectric effects can be neglected for such weak electric fields.
4. With no proof mass, nonlinear behavior is sufficiently modeled by a cubic nonlinearity, third-order damping, and linear coupling. Even with a proof mass, this model is sufficient for low base accelerations. However, higher driving amplitudes render fifth-order nonlinearities important. This is especially true for PZT-5A and for heavier proof masses.

Table 4. Regression coefficients for PZT-5H.

Regression coefficients	$\mathcal{E}_P \leq 10\%$	$\mathcal{E}_P \leq 20\%$	$\mathcal{E}_P \leq 30\%$	$\mathcal{E}_P \leq 40\%$
p_1	−4.1707	−5.2880	−6.4307	−7.7441
p_0	7.9644	10.9745	13.9298	17.4131

Table 5. Regression coefficients for PZT-5A.

Regression coefficients	$\mathcal{E}_P \leq 10\%$	$\mathcal{E}_P \leq 20\%$	$\mathcal{E}_P \leq 30\%$	$\mathcal{E}_P \leq 40\%$
p_1	−2.3145	−2.9230	−3.5569	−4.2415
p_0	4.9598	6.0000	7.0836	8.2538

Since most harvesters incorporate a proof mass for resonant frequency tunability, the results of this investigation and the scaling analysis of the section titled "Linear versus nonlinear modeling" indicate that nonlinear elasticity and damping become increasingly important. The dissipation model utilized in this study was selected over air drag in view of the nonlinear resonance curves of

piezoelectric oscillators not subject to large deformations (Samal et al., 2006b; Von Wagner, 2003). However, the high oscillation velocities may be rendering both quadratic air damping and nonlinear structural dissipation relevant. Correctly determining the physical mechanism of the harvester dissipation aside from the harvesting process is important for accurate modeling as illustrated in our results. Methods within several articles concerning atomic force microscopes immersed in fluids may be of benefit in investigating and modeling damping in piezoelectric energy harvesters (Chon et al., 2000; Cole and Clark; Sader, 1998) along with the recent work of Kamel et al. (2010). Furthermore, the presumption of linear proportional damping in a distributed parameter system itself, though the widespread norm, may require reexamination (Banks et al., 1998).

Future work is also in order pertaining to the nonlinear coupling. While this article only examined one impedance load such that low voltages were generated, larger impedance loads translate to greater electric potential fields in the electroelastic laminates and may thus render higher-order electrical effects and nonlinear coupling important. Hence, another direction for future research would be to investigate the influence of resistive loads on the nonlinear response of piezoelectric harvesters to determine at what point nonlinear coupling begins to influence the nonlinear resonance curves.

Funding

Financial support from the Duke University Center for Theoretical and Mathematical Sciences and Dr Ronald Joslin through an Office of Naval Research (ONR) Young Investigator Award is gratefully acknowledged as is support from AFOSR MURI Grant No. F-9550-06-1-0326, "Energy Harvesting and Storage Systems for Future Air Force Vehicles," monitored by Dr B.L. Lee.

References

Banks HT, Luo Z, Bergman LA, et al. (1998) On the existence of normal modes of damped discrete-continuous systems. *Journal of Applied Mechanics* 65(4): 980–990.

Chon J, Mulvaney P and Sader J (2000) Experimental validation of theoretical models for the frequency response of atomic force microscope cantilever beams immersed in fluids. *Journal of Applied Physics* 87(8): 3978.

Cole DG and Clark RL. (2007) Fluid-structure interaction in atomic force microscope cantilever dynamics and thermal response, *J. Appl. Phys.* 101, 034303.

Crandall S, Karnopp D, Kurtz E, et al. (1968) *Dynamics of Mechanical and Electromechanical Systems*. Malabar, FL: Krieger.

Crawley E and Anderson E (1990) Detailed models for the piezoceramic actuation of beams. *Journal of Intelligent Material Systems and Structures* 1(4): 4–25.

Daqaq M, Stabler C, Qaroush Y, et al. (2009) Investigation of power harvesting via parametric excitations. *Journal of Intelligent Material Systems and Structures* 20(5): 545–557.

Da Silva MC and Glynn C (1978) Nonlinear flexural-flexural-torsional dynamics of inextensional beams: I. Equations of motion. *Mechanics Based Design of Structures and Machines* 6(4): 437–448.

DuToit N, Wardle B and Kim S (2005) Design considerations for MEMS-scale piezoelectric mechanical vibration energy harvesters. *Integrated Ferroelectrics* 71: 121–160.

Erturk A and Inman D (2008a) A distributed parameter electromechanical model for cantilevered piezoelectric energy harvesters. *Journal of Vibration and Acoustics* 130: 1–15.

Erturk A and Inman D (2008b) Comment on modeling and analysis of a bimorph piezoelectric cantilever beam for voltage generation. *Smart Material Structures* 17(5), doi:10.1088/0964-1726/17/5/058001

Erturk A and Inman D (2008c) Issues in mathematical modeling of piezoelectric energy harvesters. *Smart Material Structures* 17(6): 1–14.

Erturk A and Inman D (2009a) An experimentally validated bimorph cantilever model for piezoelectric energy harvesting from base excitations. *Smart Material Structures* 18: 1–18.

Erturk A and Inman D (2009b) On mechanical modeling of cantilevered piezoelectric vibration energy harvesters. *Journal of Intelligent Material Systems and Structures* 19: 1311–1325.

Hagood N, Chung W and Von Flotow A (1990) Modelling of piezoelectric actuator dynamics for active structural control. *Journal of Intelligent Material Systems and Structures* 1(2): 327–354.

Hu Y, Xue H and Yang J (2006) Nonlinear behavior of a piezoelectric power harvester near resonance. *IEEE Transactions on Ultrasonics, Ferroelectrics, and Frequency Control* 53(7): 1387–1391.

Ikeda T (1996) *Fundamentals of Piezoelectricity*. Oxford: Oxford University Press.

Jiang S, Li X, Guo S, et al. (2005) Performance of a piezoelectric bimorph for scavenging vibration energy. *Smart Materials and Structures* 14(4): 769–774.

Kamel T, Elfrink R, Renaud M, et al. (2010) Modeling and characterization of MEMS-based piezoelectric harvesting devices. *Journal of Micromechanics and Microengineering* 20(105023): 14.

Kim JDM, Hoegen M and Wardle BL (2010) Modeling and experimental verification of proof mass effects on vibration energy harvester performance. *Smart Material Structures* 19(4): 045023.

Masana R and Daqaq M (2011) Electromechanical modeling and nonlinear analysis of axially-loaded energy harvesters. *Journal of Vibration and Acoustics* 133(1): 011007.

Maugin G (1985) *Nonlinear Electromechanical Effects and their Application*. World Scientific Publishing Co. Pte. Ltd., Singapore.

Nayfeh A and Mook D (1979) *Nonlinear Oscillations*. New York: Wiley.

Parashar S and Von Wagner U (2004) Nonlinear longitudinal vibrations of transversally polarized piezoceramics: experiments and modeling. *Nonlinear Dynamics* 37: 51–73.

Priya S, Viehland D, Carazo A, et al. (2001) High-power resonant measurements of piezoelectric materials: importance of elastic nonlinearities. *Journal of Applied Physics* 90(3): 1469–1479.

Sader J (1998) Frequency response of cantilever beams immersed in viscous fluids with applications to the

atomic force microscope. *Journal of Applied Physics* 84(1): 64–76.
Samal M, Seshu P, Parashar S, et al. (2006a) Nonlinear behaviour of piezoceramics under weak electric fields: Part-i: 3-d finite element formulation. *International Journal of Solids and Structures* 43(6): 1422–1436.
Samal M, Seshu P, Parashar S, et al. (2006b) Nonlinear behaviour of piezoceramics under weak electric fields. Part-ii: numerical results and validation with experiments. *International Journal of Solids and Structures* 43(6): 1437–1458.
Smits JG, Dalke SI and Cooney TK (1991) The constituent equations of piezoelectric bimorphs. *Sensors and Actuators A: Physical* 28(1): 41–61.
Sodano H, Park G and Inman D (2004) Estimation of electric charge output for piezoelectric energy harvesting. *Strain* 40: 49–58.
Stanton S and Mann B Nonlinear electromechanical dynamics of piezoelectric inertial generators: Modeling, analysis, and experiment. *Nonlinear Dynamics*.
Stanton S, Erturk A, Mann B, et al. (2010a) Nonlinear piezoelectricity in electroelastic energy harvesters: modeling and experimental identification. *Journal of Applied Physics* 108(1): 074903.
Stanton S, Erturk A, Mann B, et al. (2010b) Resonant manifestation of intrinsic nonlinearity in electroelastic micropower generators. *Applied Physics Letters* 97: 254101.
Tiersten H (1993) Electroelastic equations for electroded thin plates subject to large driving voltages. *Journal of Applied Physics* 74(5): 3389–3393.
Triplett A and Quinn D (2009) The effect of non-linear piezoelectric coupling on vibration-based energy harvesting. *Journal of Intelligent Material Systems and Structures* 20(16): 1959–1967.
Von Wagner U (2003) Non-linear longitudinal vibrations of piezoceramics excited by weak electric fields. *International Journal of Nonlinear Mechanics* 38(4): 565–574.
Von Wagner U and Hagendorn P (2002) Piezo-beam systems subjected to weak electric field: experiments and modeling of nonlinearities. *Journal of Sound and Vibration* 256(5): 861–872.
Yang J (2005) *Analysis of Piezoelectric Devices*. New York: Springer.
Yu S, He S and Li W (2010) Theoretical and experimental studies of beam bimorph piezoelectric power harvesters. *Journal of Mechanics and Materials of Structures* 5(3): 427–445.
Zhang W and Meng G (2005) Nonlinear dynamical system of micro-cantilever under combined parametric and forcing excitations in MEMS. *Sensors and Actuators A: Physical* 119(2): 291–299.

Appendix I

Definition of modal coefficients

$$M = b\left(\rho_b h_b + 2\rho_p h_p\right) b \int_0^L \phi^2 \,\mathrm{d}x + M_t \phi(L)^2 + J_o \phi'(L)^2 \tag{A.1}$$

$$K = \left(c_{xx,b} I_b + 2c_{xx}^E I_p\right) \int_0^L \phi''^2 \,\mathrm{d}x \tag{A.2}$$

$$G = \frac{1}{240} c_4^E b h_p \left(16h_p^4 + 40h_p^3 h_s + 40h_p^2 h_s^2 + 20h_p h_s^3 + 5h_s^4\right) \times \int_0^L \phi^4 \,\mathrm{d}x \tag{A.3}$$

$$\Theta = \frac{1}{2}\tilde{\Theta} = \frac{1}{2} b e_{31} \left(h_p + h_s\right) \phi'(L) \tag{A.4}$$

$$C = h_p^{-1} \tilde{C} = \varepsilon_{ZZ}^S \left(\frac{bL}{2h_p}\right) \tag{A.5}$$

$$F_g = g\left[\left(\rho_b h_b + 2\rho_p h_p\right) b \int_0^L \phi \,\mathrm{d}x + M_t \phi(L)\right] \tag{A.6}$$

$$D_a = \left(\eta_b I_b + 2\eta_p I_p\right) \int_0^L \phi''^2 \,\mathrm{d}x \tag{A.7}$$

$$D_b = \frac{3}{40} \zeta b h_p \left(16h_p^4 + 40h_p^3 h_s + 40h_p^2 h_s^2 + 20h_p h_s^3 + 5h_s^4\right) \int_0^L \phi''^4 \mathrm{d}x \tag{A.8}$$

$$D_d = \frac{1}{2}\tilde{\Lambda} = \frac{1}{2} \gamma b \left(h_p + h_s\right) \phi'(L) \tag{A.9}$$

$$D_e = \frac{1}{2}\chi = \nu\left(\frac{bL}{2h_p}\right) \tag{A.10}$$